

Fig 1. Schematic depiction of the monochromatic SR system. **A**, Illustration of the experimental arrangement for SR microangiography at BL28B2. **B**, Photon mass attenuation coefficient of barium (blue line) and liquid water (red line). Monochromatic x-ray energy is adjusted to 37.5 keV, just above the barium K-edge energy to produce the highest contrast image.

Microangiography and Image Analysis

Microangiographic images of mouse brain were obtained by using monochromatic SR in the Japan Synchrotron Radiation Research Institute (SPring-8, Hyogo, Japan).^{4,8} There are 3 large 3rd-generation synchrotron radiation facilities in the world: the Advanced Photon Source in Argonne (United States), the European Synchrotron Radiation Facility in Grenoble (France), and SPring-8 (the latter was used for the studies described herein). These facilities are open to scientists in many fields, including material, chemical, and life sciences investigators. The experimental setup for x-ray imaging by using monochromatic SR at the SPring-8 BL28B2 beamline is shown in Fig 1A. The storage ring was operated at 8-GeV electron beam energy, and beam current was 80–100 mA. The distance between the point source in the bending magnet and the detector was ~45 m. A nearly parallel x-ray beam was used for imaging without blurring because of the small size of the x-ray source and the very long source-to-object distance. The single crystal monochromator selects a single energy of synchrotron radiation. The shutter system is located between the monochromator and the object. X-rays transmitted through the object are detected by an x-ray direct-conversion-type detector incorporating the x-ray saticon pickup tube. Monochromatic x-ray energy was adjusted to 37.5 keV, just above the barium K-edge energy, to produce the highest contrast image of the barium (Fig 1B). X-ray flux at the object position was around 1×10^{10} photons/mm² per second in imaging experiments. The images were acquired as 1024×1024 pixels with 10-bit resolution after analog-to-digital conversion. The FOV was 4.5×4.5 mm², and pixel size was ~4.5 μm.^{9,10}

Mammographic Images

To compare spatial and contrast resolution, we obtained mammographic images, which are known for having the highest resolution in clinical applications,¹¹ of murine brains. Digital images were captured at an energy level of 24 kV by using a molybdenum target and a molybdenum filter with 90° cranial projection. Source-to-image distance was 65 cm.

Induction of Focal Cerebral Ischemia

Permanent focal cerebral infarction was induced by ligation and disconnection of the left MCA of male SCID mice ($n = 5$), as described.^{12–14} Briefly, under inhaled halothane (3%) anesthesia, animals were placed on their right sides and a skin incision was made at the midpoint between the left orbit and the external auditory canal. The temporalis muscle was incised, and the zygomatic arch was removed to expose the squamous portion of the temporal bone. Using a dental drill, we made a small hole above the distal portion, M1, of the MCA, which could be seen through the exposure in the skull. The dura mater was opened, and the left MCA was electrocauterized and disconnected just distal to its crossing of the olfactory tract. Body temperature was maintained at 36.5°–37°C by using a heat lamp during the operation and for 2 hours after MCA occlusion. Cerebral blood flow (CBF) in the left MCA area was measured by laser-Doppler flowmetry (Advance, Tokyo, Japan). The holding device of the laser probe (ALF probe; Neuroscience, Osaka, Japan) (1.5 mm in diameter, 7.0 mm in length) was secured on the cranium at a site located above the ischemic core of the left MCA area (approximately 1 mm anterior and 5 mm distal to the bregma), and CBF was monitored during the procedure and 24 hours after ligation of the MCA. Mice displaying a decrease in CBF by ~75% immediately after the procedure and thereafter for an additional 24 hours were used for experiments.¹⁵ Nine days after induction of cerebral ischemia, the cerebral microcirculation was examined by SR imaging.

MR Imaging System

To confirm cerebral infarction consequent to ligation of the MCA, we performed MR imaging on day 2 poststroke. MR imaging used a 2T compact MR imaging system with a permanent magnet (MRmini SA206, Dainippon Sumitomo Pharma, Osaka, Japan) by using a radio-frequency solenoid coil for signal-intensity detection. For each imaging sequence, 15 coronal images were acquired with a section thickness of 1 mm, gapped at 0.5 mm. T1-weighted spin-echo MR images were acquired with a TR/TE of 500/9 ms, a FOV of 36.6×18.3 mm, an image acquisition matrix of 256×128 , and NEX, 4. T2-weighted spin-echo MR images were obtained with TR/TE, 3000/69, 256×128 , and NEX, 2. Because the sequences to obtain diffusion-weighted images by using this machine are still in development, we evaluated the cerebral ischemia by T2-weighted images on day 2 poststroke.

Data Analysis

In all experiments, the mean \pm SE is reported.

Results

Visualization of Cerebral Arteries by SR Imaging

After euthanasia and systemic perfusion with PBS, barium sulfate particles were infused via the left ventricle of the heart. As shown in Fig 2A, cerebral arteries on the brain surface were filled with contrast medium. First, we investigated vascular

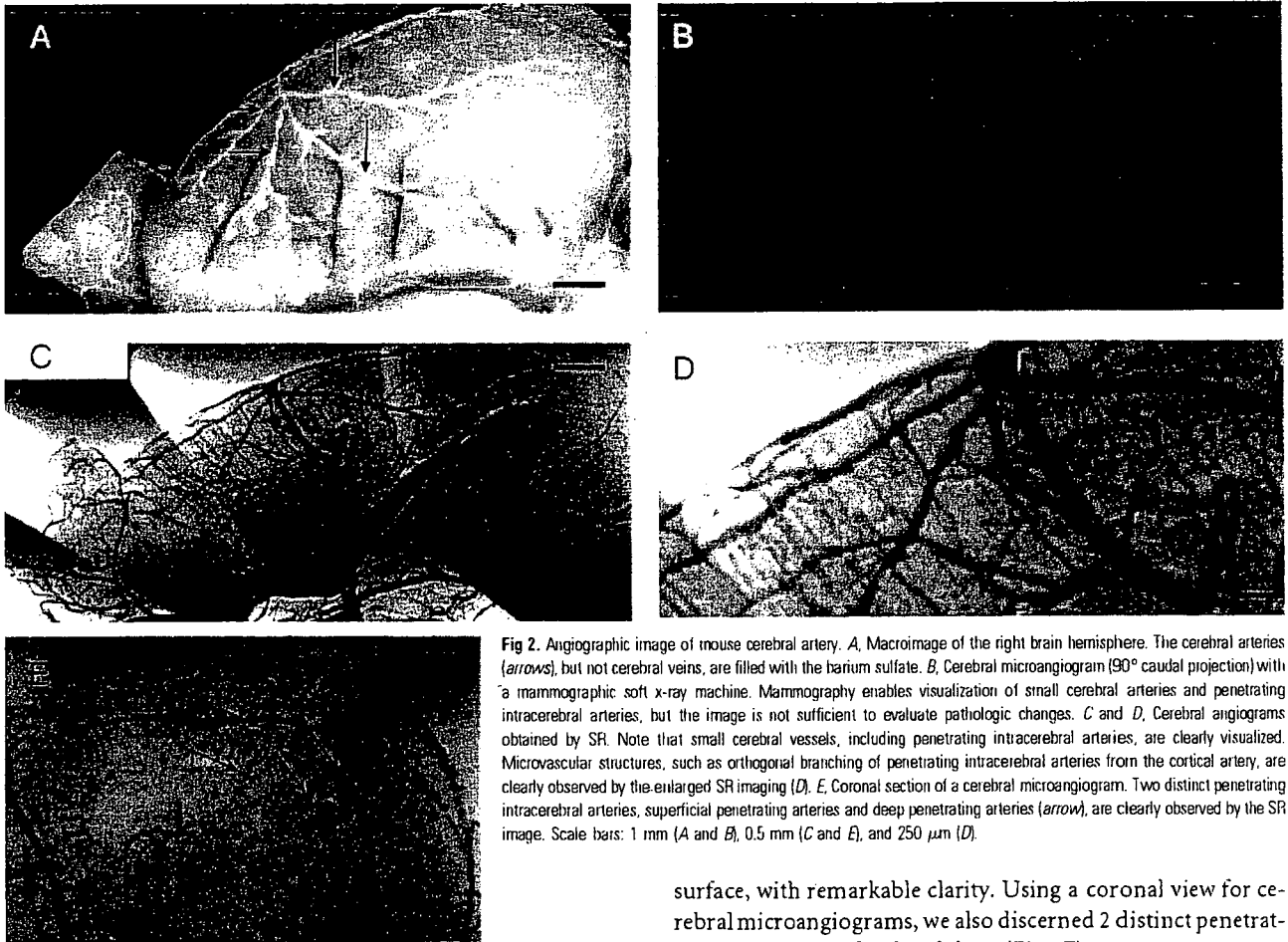


Fig 2. Angiographic image of mouse cerebral artery. *A*, Macroimage of the right brain hemisphere. The cerebral arteries (arrows), but not cerebral veins, are filled with the barium sulfate. *B*, Cerebral microangiogram (90° caudal projection) with a mammographic soft x-ray machine. Mammography enables visualization of small cerebral arteries and penetrating intracerebral arteries, but the image is not sufficient to evaluate pathologic changes. *C* and *D*, Cerebral angiograms obtained by SR. Note that small cerebral vessels, including penetrating intracerebral arteries, are clearly visualized. Microvascular structures, such as orthogonal branching of penetrating intracerebral arteries from the cortical artery, are clearly observed by the enlarged SR imaging (*D*). *E*, Coronal section of a cerebral microangiogram. Two distinct penetrating intracerebral arteries, superficial penetrating arteries and deep penetrating arteries (arrow), are clearly observed by the SR image. Scale bars: 1 mm (*A* and *B*), 0.5 mm (*C* and *E*), and 250 μm (*D*).

images by mammography (Fig 2*B*). However, sufficient spatial and contrast resolution was not obtained by mammographic imaging to evaluate the angioarchitecture of small cerebral vasculature. Peripheral branches of the MCA (75–100 μm in diameter) and small vessels emerging from peripheral branches were barely visualized.

Next, we investigated the vascular profile by using SR (Fig 2*C*, normal view; *D*, enlarged view). At the brain surface, cortical arteries branching from the MCA and pial arteries, $\sim 30 \mu\text{m}$ in diameter, were clearly visualized. Within the brain parenchyma, penetrating intracerebral arteries, branching orthogonally from cortical or pial arteries, were also observed. The interval between intracerebral arteries was $126.1 \pm 35.5 \mu\text{m}$ ($n = 20$), the diameter of the proximal side of the intracerebral arteries was $29.5 \pm 3.1 \mu\text{m}$ ($n = 20$), and each intracerebral artery was observed to progressively narrow to a diameter below the limit of resolution (10 μm). Vascular diameters determined by SR imaging of intracerebral arteries and small arterial branches were identical to those observed in previous pathologic studies of murine brain.¹⁶ Using SR imaging, we could discern 2 types of intracerebral arteries: superficial penetrating arteries perfusing only the cortical area and penetrating arteries reaching the subcortical area and perfusing the deep white matter. These vascular structures observed in murine brain by SR imaging are similar to previous observations in human anatomic studies.^{17–20} Compared with mammographic images, SR imaging enabled visualization of penetrating intracerebral arteries (diameter range of 10–30 μm), as well as small peripheral branches of MCA at the brain

surface, with remarkable clarity. Using a coronal view for cerebral microangiograms, we also discerned 2 distinct penetrating arteries, superficial and deep (Fig 2*E*).

SR Images after Cerebral Infarction

To evaluate cerebral vasculature in the context of pathologic changes, cerebral infarction was induced by ligation of the MCA. The area of cerebral infarction was visualized by MR imaging on day 2 after induction of stroke. As we have shown previously by 2,3,5-triphenyltetrazolium staining,¹² limited cortical infarction was observed in the MCA area on T2-weighted images (Fig 3*A*). In contrast, no hyper- or hypointense region was observed on T1-weighted images (Fig 3*B*), indicating the absence of bleeding or parenchymal injury. Although no morphologic (Fig 3*C*) or vascular structural (Fig 3*D*) changes were observed in the right hemisphere (non-stroke side), by day 9 after MCA occlusion, tissue degradative changes were observed in the cortical and shallow white matter of the left MCA area (stroke side, Fig 3*E*). To evaluate the integrity of the microvasculature after stroke, we obtained SR images. The number of penetrating intracerebral arteries dramatically decreased, though cortical branches at the brain surface could still be visualized (Fig 3*F*). On the coronal view, the disappearance of the intracerebral arteries on the ischemic side was also clearly observed (Fig 3*G*).

Discussion

Cerebral artery disease in small vessels is a major cause of cerebral infarction and hemorrhage. Although pathologic changes in small arteries have been reported on the basis of microscopic analysis, it has been difficult to assess the mor-

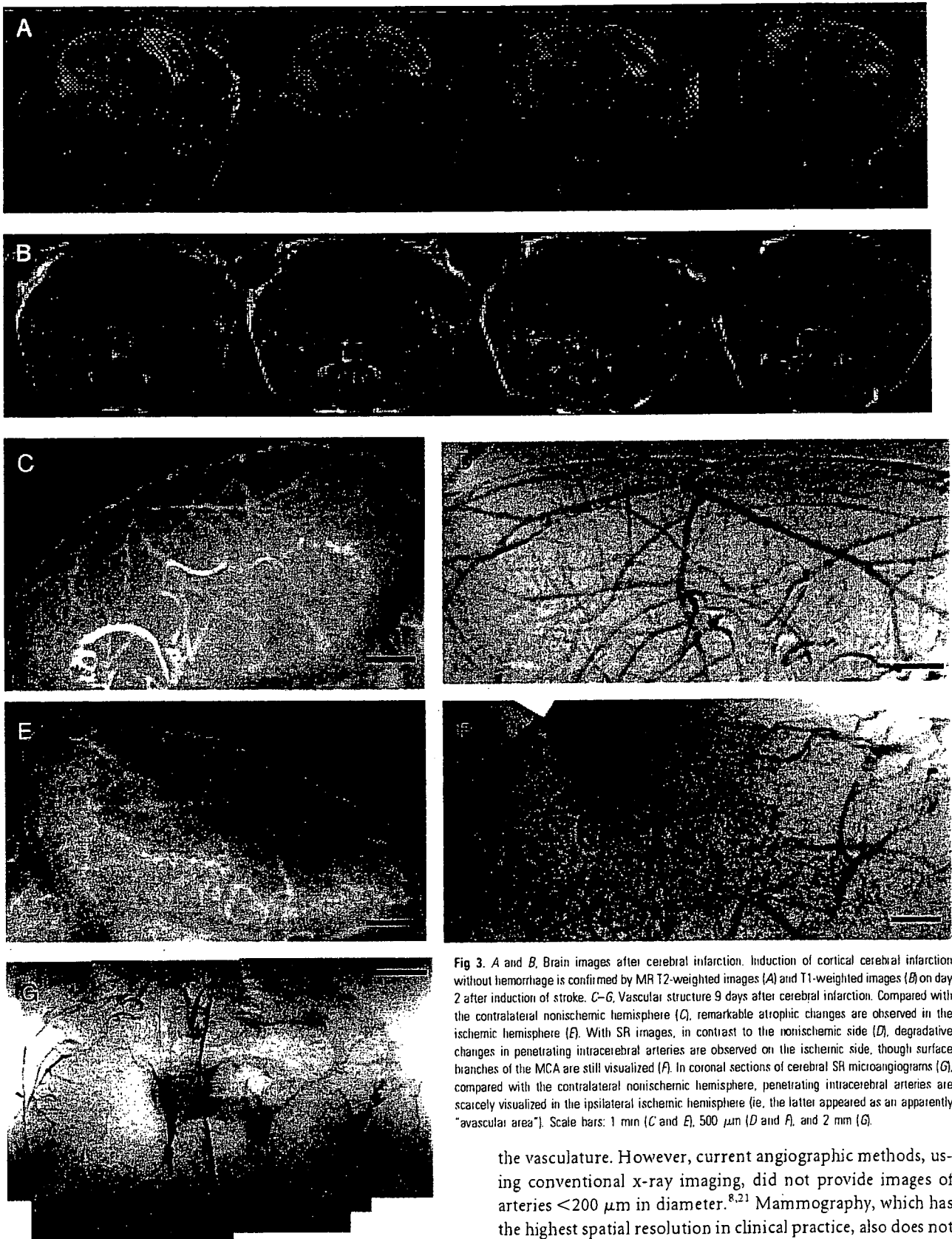


Fig 3. *A and B*, Brain images after cerebral infarction. Induction of cortical cerebral infarction without hemorrhage is confirmed by MR T2-weighted images (*A*) and T1-weighted images (*B*) on day 2 after induction of stroke. *C–G*, Vascular structure 9 days after cerebral infarction. Compared with the contralateral nonischemic hemisphere (*C*), remarkable atrophic changes are observed in the ischemic hemisphere (*E*). With SR images, in contrast to the nonischemic side (*D*), degradative changes in penetrating intracerebral arteries are observed on the ischemic side, though surface branches of the MCA are still visualized (*F*). In coronal sections of cerebral SR microangiograms (*G*), compared with the contralateral nonischemic hemisphere, penetrating intracerebral arteries are scarcely visualized in the ipsilateral ischemic hemisphere (ie, the latter appeared as an apparently “avascular area”). Scale bars: 1 mm (*C* and *E*), 500 μm (*D* and *F*), and 2 mm (*G*).

phology of small cerebral vessels in situ through imaging studies. Herein, we demonstrate that small cerebral vessels can be clearly visualized by microangiography by using SR.

Conventional angiography is commonly used to evaluate

the vasculature. However, current angiographic methods, using conventional x-ray imaging, did not provide images of arteries $<200 \mu\text{m}$ in diameter.^{8,21} Mammography, which has the highest spatial resolution in clinical practice, also does not have sufficient resolution to visualize small vessels with a diameter of $<50 \mu\text{m}$.¹¹ Microangiographic techniques have been developed by using fine-focus x-rays and sensitive films to evaluate the microcirculation in the brain.²⁰ These methods enable visualization of human cortical perforating arteries and

medullary long branches (100 μm in diameter) by using 1-cm-thick sections of brain.²⁰ However, the limit of detection by using these methods applied to thick sections has been reported to be vessels of 50 μm in diameter.²² Furthermore, visualization of smaller arteries required thin sections cut with a microtome.²⁰ The latter method is not well-suited to the evaluation of 3D cerebral vascular trees.

Compared with these conventional methods, the principal advantage of SR is the small size of the electron beam, thereby providing a high-intensity x-ray point source. Using a nearly parallel beam of SR, along with a precise detection system (pixel size of 4.5 μm), allowed us to obtain high-quality angiographic images with excellent spatial resolution. Furthermore, setting SR at an energy level just above the K absorption of barium produced the highest contrast images. SR imaging provides a powerful tool to reveal the morphology of small cerebral arteries such as superficial and deep penetrating arteries, allowing analysis of their physiologic and pathologic properties under a variety of conditions (ie, borderzone in infarction^{23,24} and microaneurysm formation).

Fluorescence microscopy is another tool potentially useful for analysis of the microcirculation.²⁵ Although fluorescence microscopy provides visualization of microcirculation at the brain surface, the advantage of SR imaging is visualization of small vessels that have penetrated into the brain parenchyma, such as the subcortex. In addition, SR imaging allows performance of microangiography with an optimal projection. When the latter is combined with a microinjector, sequential real-time images can be obtained, providing the substrate for hemodynamic analysis.

In this article, we investigated SR imaging after stroke and showed that the SR image reflects pathologic changes previously observed by using anatomic/microscopic analysis. On day 9 after MCA occlusion, arteries on the surface of the cerebrum were visualized by SR, though penetrating intracerebral arteries were not detected. Previous studies have shown that the integrity of the distal cortical artery is usually maintained after occlusion of the proximal artery and that collateral flow is established through expansion of previously existing and/or formation of new vascular channels.^{25,26} Analysis with enhanced MR imaging has shown cerebral parenchymal enhancement in the stroke area by 1 week after cerebral infarction,²⁷ indicative of blood flow in the peri-ischemic area. In contrast, penetrating intracerebral arteries were dramatically decreased in number in the ischemic hemisphere, though cortical branches on the brain surface were maintained after MCA occlusion. It has previously been shown that microvasculature in the ischemic territory displays adhesion of polymorphonuclear leukocytes in postcapillary venules, followed by the disruption of the microvascular network.²⁸ These previous findings are consistent with the results of our vascular images obtained by SR after ligation of the MCA.

Conclusion

Our study demonstrates, for the first time, the morphologic features of small vascular networks in murine brain by microangiography by using SR imaging. Our approach provides a powerful tool for evaluating potential angiogenic/antiangiogenic therapeutic strategies, as well as pathologic examination of the cerebral microarterial tree.

Acknowledgments

We thank Y. Kasahara, K. Tomiyasu, and M. Aoki for technical assistance.

References

- Phillips SJ, Whisnant JP. Hypertension and the brain: The National High Blood Pressure Education Program. *Arch Intern Med* 1992;152:938-45
- Ito K, Tanaka E, Mori H, et al. A microangiographic technique using synchrotron radiation to visualize dermal circulation in vivo. *Plast Reconstr Surg* 1998;102:1128-33
- Tokiya R, Umetani K, Imai S, et al. Observation of microvasculatures in athymic nude rat transplanted tumor using synchrotron radiation microangiography system. *Academic Radiology* 2004;9:1039-46
- Takeshita S, Ishiki T, Mori H, et al. Use of synchrotron radiation microangiography to assess development of small collateral arteries in a rat model of hindlimb ischemia. *Circulation* 1997;95:805-08
- Conway JG, Popp JA, Thurman RG. Microcirculation in periportal and pericentral regions of lobule in perfused rat liver. *Am J Physiol* 1985;249:G449-56
- Stock RJ, Cilento EV, McCuskey RS. A quantitative study of fluorescein isothiocyanate-dextran transport in the microcirculation of the isolated perfused rat liver. *Hepatology* 1989;9:75-82
- Birngruber R, Schmidt-Erfurth U, Teschner S, et al. Confocal laser scanning fluorescence topography: a new method for three-dimensional functional imaging of vascular structures. *Graefes Arch Clin Exp Ophthalmol* 2000;238:559-65
- Mori H, Hyodo K, Tanaka E, et al. Small-vessel radiography in situ with monochromatic synchrotron radiation. *Radiology* 1996;201:173-77
- Umetani K, Yagi N, Suzuki Y, et al. Observation and analysis of microcirculation using high-spatial-resolution image detectors and synchrotron radiation. *Proceeding of SPIE* 2000;3977:522-33
- Yamashita T, Kawashima S, Ozaki M, et al. Images in cardiovascular medicine: mouse coronary angiograph using synchrotron radiation microangiography. *Circulation* 2002;105:E3-4
- Kuzmiak CM, Pisano ED, Cole EB, et al. Comparison of full-field digital mammography to screen-film mammography with respect to contrast and spatial resolution in tissue equivalent breast phantoms. *Med Phys* 2005;32:3144-50
- Taguchi A, Soma T, Tanaka H, et al. Administration of CD34+ cells after stroke enhances neurogenesis via angiogenesis in a mouse model. *J Clin Invest* 2004;114:330-38
- Furuya K, Kawahara N, Kawai K, et al. Proximal occlusion of the middle cerebral artery in C57Black6 mice: relationship of patency of the posterior communicating artery, infarct evolution, and animal survival. *J Neurosurg* 2004;100:97-105
- Kitagawa K, Matsumoto M, Mabuchi T, et al. Deficiency of intercellular adhesion molecule 1 attenuates microcirculatory disturbance and infarction size in focal cerebral ischemia. *J Cereb Blood Flow Metab* 1998;18:1336-45
- Matsushita K, Matsuyama T, Nishimura H, et al. Marked, sustained expression of a novel 150-kDa oxygen-regulated stress protein, in severely ischemic mouse neurons. *Brain Res Mol Brain Res* 1998;60:98-106
- Coyne EF, Ngai AC, Meno JR, et al. Methods for isolation and characterization of intracerebral arterioles in the C57/BL6 wild-type mouse. *J Neurosci Methods* 2002;120:145-53
- Herman LH, Ostrowski AZ, Gurdjian ES. Perforating branches of the middle cerebral artery: an anatomical study. *Arch Neurol* 1963;8:32-34
- Kaplan HA. The lateral perforating branches of the anterior and middle cerebral arteries. *J Neurosurg* 1965;23:305-10
- de Reuck J. The area of the deep perforating branches of the median cerebral artery in man [in French]. *Acta Anat (Basel)* 1969;74:30-35
- Salamon G, Combalbert A, Faure J, et al. Microangiographic study of the arterial circulation of the brain. *Prog Brain Res* 1968;30:33-41
- Mori H, Hyodo K, Tobita K, et al. Visualization of penetrating transmural arteries in situ by monochromatic synchrotron radiation. *Circulation* 1994;9:863-71
- Salamon G, Raybaud C, Michotey P, et al. Angiographic study of cerebral convolutions and their area of vascularization [in French]. *Rev Neurol (Paris)* 1975;131:259-84
- Bogousslavsky J, Regli F. Centrum ovale infarcts: subcortical infarction in the superficial territory of the middle cerebral artery. *Neurology* 1992;42:1992-98
- Donnan GA, Norrving B, Bamford JM, et al. Subcortical infarctions: classification and terminology. *Cerebrovasc Dis* 1993;3:248-51
- Tomita Y, Kubis N, Calando Y, et al. Long-term in vivo investigation of mouse cerebral microcirculation by fluorescence confocal microscopy in the area of focal ischemia. *J Cereb Blood Flow Metab* 2005;25:858-67
- Zulch KJ. *Cerebral Circulation and Stroke*. Berlin, Germany: Springer-Verlag; 1971:116
- Merten CL, Knitelius HO, Assheuer J, et al. MRI of acute cerebral infarcts: increased contrast enhancement with continuous infusion of gadolinium. *Neuroradiology* 1999;41:242-48
- del Zoppo GJ, Mabuchi T. Cerebral microvessel responses to focal ischemia. *J Cereb Blood Flow Metab* 2003;23:879-94

Intense clean characteristic flash x-ray irradiation from an evaporating molybdenum diode

Michiaki Sagae

Eiichi Sato, MEMBER SPIE

Iwate Medical University

Department of Physics

3-16-1 Honchodori

Morioka 020-0015, Japan

E-mail: msagae@iwate-med.ac.jp

Etsuro Tanaka

Tokyo University of Agriculture

Department of Nutritional Science

Faculty of Applied Bioscience

1-1-1 Sakuragaoka

Setagaya-ku 156-8502, Japan

Hidezo Mori

National Cardiovascular Center Research Institute

Department of Cardiac Physiology

5-7-1 Fujishirodai, Suita

Osaka 565-8565, Japan

Toshiaki Kawai, MEMBER SPIE

Hamamatsu Photonics K. K.

Electron Tube Division 2

314-5 Shimokanzo

Iwata 438-0193, Japan

Takashi Inoue

Akira Ogawa

Iwate Medical University

Department of Neurosurgery

School of Medicine

19-1 Uchimarui

Morioka 020-8505, Japan

Shigehiro Sato

Iwate Medical University

Department of Microbiology

School of Medicine

19-1 Uchimarui

Morioka 020-8505, Japan

Kazuyoshi Takayama, MEMBER SPIE

Tohoku University

Shock Wave Research Center

Institute of Fluid Science

2-1-1 Katahira

Sendai 980-8577, Japan

Jun Onagawa

Hideaki Ido

Tohoku Gakuin University

Department of Applied Physics and Informatics

Faculty of Engineering

1-13-1 Chuo

Tagajo 985-8537, Japan

Abstract. In a flash x-ray generator, a 150-nF condenser is charged up to 80 kV by a power supply, and flash x-rays are produced by the discharge. The x-ray tube is a demountable diode, and the turbomolecular pump evacuates air from the tube with a pressure of approximately 1 mPa. Since the electric circuit of the high-voltage pulse generator employs a cable transmission line, the high-voltage pulse generator produces twice the potential of the condenser charging voltage. Because bremsstrahlung rays are not emitted in the opposite direction of that of electron trajectory, clean molybdenum K-series characteristic x-rays can be produced without using a filter. When the charging voltage is increased, the K-series characteristic x-ray intensities of molybdenum increase. The K lines are clean and intense, and hardly any bremsstrahlung rays are detected. The x-ray pulse widths are approximately 100 ns, and the time-integrated x-ray intensity has a value of approximately 500 μ Gy per pulse at 1.0 m from the x-ray source, with a charging voltage of 80 kV. © 2007 Society of Photo-Optical Instrumentation Engineers. [DOI: 10.1117/1.2541668]

Subject terms: flash x-ray; energy-selective radiography; characteristic x-rays; quasi-monochromatic x-rays; bremsstrahlung x-ray distribution.

Paper 050104R received Feb. 7, 2005; revised manuscript received Jan. 10, 2006; accepted for publication Aug. 10, 2006; published online Mar. 2, 2007. This paper is a revision of a paper presented at the SPIE conference on 26th International Congress on High-Speed Photography and Photonics, Sep. 2004, Alexandria, Virginia. The paper presented there appears (unrefereed) in SPIE proceedings Vol. 5580.

1 Introduction

In recent years, there have been several investigations dealing with the production of monochromatic x-rays in radiology and cardiology. Particularly, monochromatic parallel beams using synchrotrons have been employed to perform enhanced K-edge angiography^{1,2} and x-ray phase imaging.^{3,4} In angiography, parallel beams with photon energies of approximately 35 keV have been employed, since these beams are absorbed effectively by an iodine-based contrast medium. Subsequently, in cases where phase imaging is employed, the spatial resolution can be improved, and the number of tissues that can be observed using x-rays increases.

We have developed several different soft flash x-ray generators⁵⁻¹¹ with photon energy of less than 150 keV corresponding to specific radiographic objectives, and a major goal in our research is the development of an intense and clean monochromatic x-ray generator that can impact applications with medical radiography. Recently, we have succeeded in producing intense K-series characteristic x-rays from the axial direction of linearly evaporating targets.¹²⁻¹⁶ In metal vapor, bremsstrahlung spectra with photon energies of higher than the K-absorption edge are effectively absorbed and are converted into fluorescent x-rays. The vapor then transmits the fluorescent rays easily. However, the bremsstrahlung x-rays are produced using a molybdenum target,¹² since high-photon-energy bremsstrahlung x-rays are not absorbed effectively in the linear vapor.

To produce clean characteristic x-rays of molybdenum, silver, cerium, ytterbium, and tungsten, we have developed a compact and weak flash x-ray generator,¹⁷ and succeeded in producing clean molybdenum K-series characteristic x-rays of approximately 1×10^7 photons/cm² at 1.0 m per pulse using the angle dependence of bremsstrahlung x-rays, since bremsstrahlung rays are not emitted in the opposite direction to that of electron trajectory. Therefore, the K photons should be maximized by increasing both the tube voltage and current, and monochromatic K α rays are selected using a zirconium filter.¹⁸ Furthermore, both the bremsstrahlung and characteristic x-rays are produced in a metal vapor, and the vapor transmits K-series characteristic x-rays easily. Thus, we are very interested in the x-ray characteristics of a diode with an evaporating target formed by increasing the electrostatic energy in a high-voltage condenser.

In this work, we developed a new flash x-ray generator utilizing a ring-cathode molybdenum diode, used to perform a preliminary experiment for generating intense and clean K-series characteristic x-rays from an evaporated molybdenum target tip utilizing the angular dependence of the bremsstrahlung x-ray distribution.

2 Generator

2.1 High-Voltage Circuit

Figure 1 shows a block diagram of an intense flash x-ray generator. The generator consists of the following essential components: a high-voltage power supply, a high-voltage condenser with a capacity of approximately 150 nF, an air gap switch, a turbomolecular pump, a thyatron pulse generator as a trigger device, and a flash x-ray tube. In this

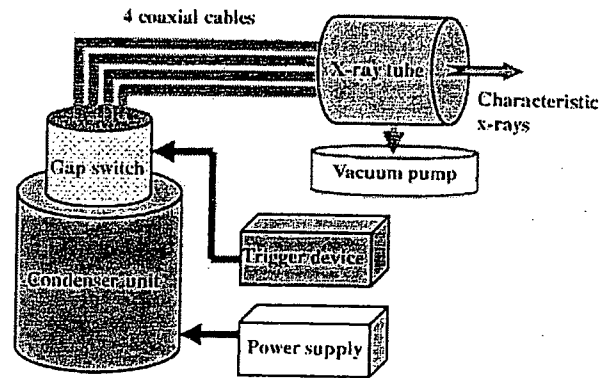


Fig. 1 Block diagram of the intense characteristic flash x-ray generator with a ring-cathode molybdenum diode.

generator, a four-cable transmission line is employed to increase maximum tube voltage using high-voltage reflection and to decrease the impedance of the generator. The high-voltage main condenser is charged up to 80 kV by the power supply, and electric charges in the condenser are discharged to the tube through the four cables after closing the gap switch with the trigger device (Fig. 2).

2.2 X-Ray Tube

The x-ray tube is a demountable cold-cathode diode that is connected to the turbomolecular pump with a pressure of approximately 1 mPa (Fig. 3). This tube consists of the following major parts: a ring-shaped graphite cathode with an inside diameter of 4.5 mm, a stainless-steel vacuum chamber, a nylon insulator, a polyethylene terephthalate (Mylar) x-ray window 0.25 mm in thickness, and a rod-shaped molybdenum target 3.0 mm in diameter. The distance between the target and cathode electrodes can be regulated from the outside of the tube, and is set to 1.5 mm. As electron beams from the cathode electrode are roughly converged to the target by the electric field in the tube, the vapor x-ray source forms at the solid target tip. Because bremsstrahlung rays are not emitted in the opposite direction to that of the electron trajectory (Fig. 4), clean molybdenum K-series characteristic x-rays can be produced without using a molybdenum filter.

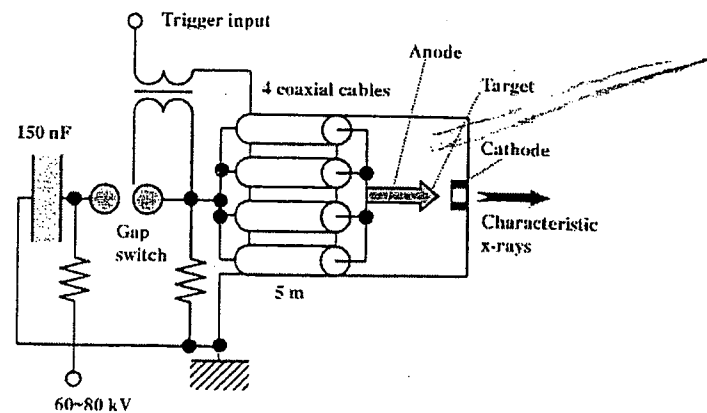


Fig. 2 Circuit diagram of the flash x-ray generator utilizing a coaxial transmission line.

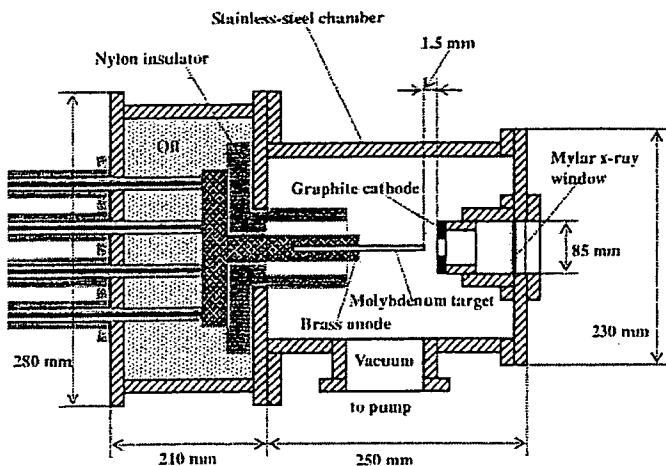


Fig. 3 Schematic drawing of the flash x-ray tube with a rod-shaped molybdenum target and a ring graphite cathode.

3 Characteristics

3.1 Tube Voltage and Current

In this generator, it was difficult to measure the tube voltage and current, since the tube voltages were high and there was no space to set a current transformer for measuring the tube current. The voltage and current roughly display damped oscillations. When the charging voltage is increased, both the maximum tube voltage and current increase. At a charging voltage of 80 kV, the estimated maximum values of the tube voltage and current are approximately 160 kV (two times the charging voltage) and 40 kA, respectively.

3.2 X-Ray Output

The x-ray output pulse was detected using a combination of a plastic scintillator and photomultiplier (Fig. 5). Due to photoelectric transfer characteristics, the pulse height was not proportional to the x-ray intensity. The x-ray pulse height increased with corresponding increases in the charge-

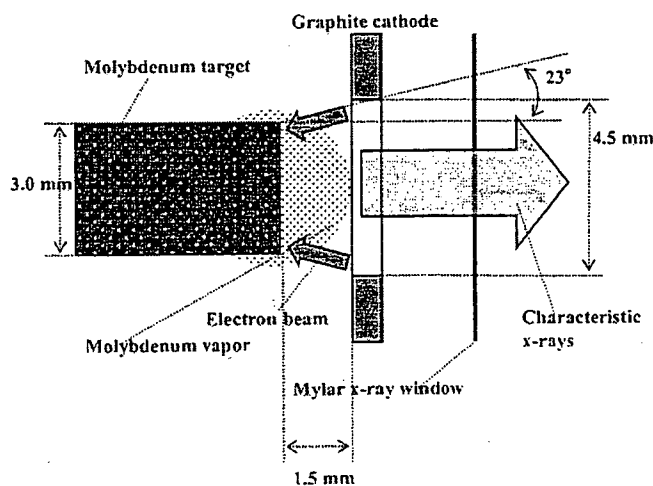


Fig. 4 Irradiation of characteristic x-rays using the angle dependence of bremsstrahlung x-ray intensity distribution. Bremsstrahlung rays are not emitted in the opposite direction of that of electron trajectory.

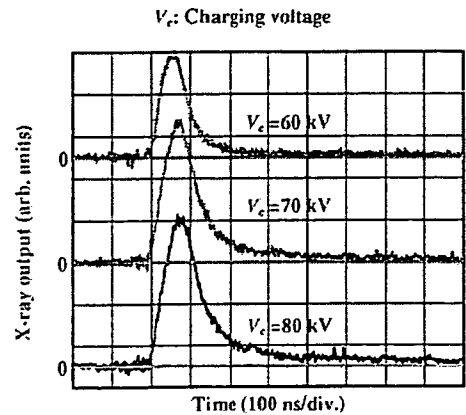


Fig. 5 X-ray outputs detected using a combination of a plastic scintillator and photomultiplier.

ing voltage. The x-ray pulse widths were approximately 100 ns, and the time-integrated x-ray intensity measured by a thermoluminescence dosimeter (Kyokko TLD Reader 1500 having MSO-S elements without energy compensation) had a value of approximately 500 μ Gy per pulse at 1.0 m from the x-ray source, with a charging voltage of 80 kV.

3.3 X-Ray Source

To observe the characteristic x-ray source, we employed a 100- μ m-diam pinhole camera and an x-ray film (Polaroid XR-7) (Fig. 6). When the charging voltage was increased, both spot dimension and intensity increased. Because the maximum diameter was larger than the target diameter of 3.0 mm, the vapor x-ray source formed at the solid target tip.

3.4 X-Ray Spectra

X-ray spectra were measured by a transmission-type spectrometer with a lithium fluoride curved crystal 0.5 mm in thickness. The spectra were taken by a computed radiography (CR) system (Konica Regius 150)¹⁹ with a wide dynamic range, and relative x-ray intensity was calculated from Dicom digital data. Using this spectrometer, it is easy to measure low intensity bremsstrahlung x-rays.^{12,20} Figure

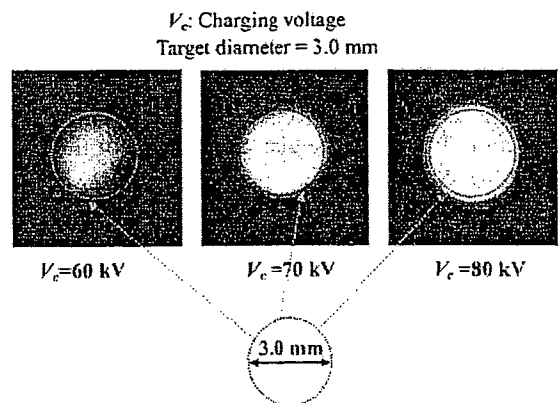


Fig. 6 Images of the characteristic x-ray source measured using a pinhole camera with changes in the charging voltage.

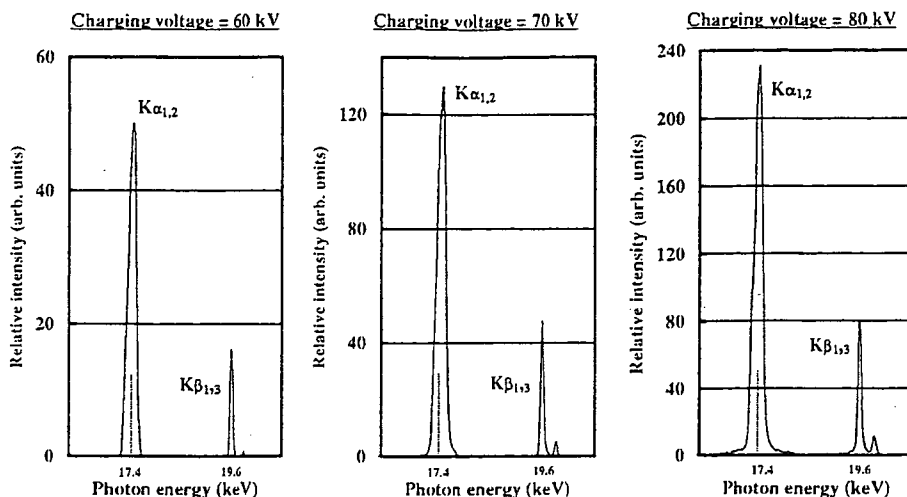


Fig. 7 X-ray spectra from the molybdenum target. The spectra were measured using a transmission-type spectrometer with a lithium fluoride curved crystal.

7 shows measured spectra from the molybdenum target. We observed clean K-series lines, while bremsstrahlung rays were hardly detected at all. The characteristic x-ray intensity substantially increased with increases in the charging voltage.

4 Flash Radiography

The quasi-monochromatic flash radiography was performed by the CR system at 1.2 m from the x-ray source, and the distance between the radiographic object and the imaging plate of the CR was 0 m. First, rough measurements of spatial resolution were made using wires. Figure 8 shows radiograms of tungsten wires coiled around a pipe made of polymethyl methacrylate with a charging voltage (V_c) of 70 kV. Although the image contrast increased with increases in the wire diameter, a 50- μ m-diam wire could be observed.

Figure 9 shows a radiogram of a vertebra with a V_c of 70 kV; fine structures in the vertebra were observed. Next, the image of water spouted from an injector is shown in Fig. 10. This image was taken with the slight addition of an iodine-based contrast medium with a V_c of 80 kV. Because the x-ray duration was about 100 ns, the stop-motion image of water could be obtained. Figures 11 and 12 show angio-

grams of a rabbit heart ($V_c=70$ kV) and thigh ($V_c=80$ kV), respectively. In angiography, iodine-based microspheres 15 μ m in diameter were used, and fine blood vessels of about 100 μ m were visible.

5 Discussion and Conclusions

Concerning spectrum measurement, we obtain fairly clean molybdenum $K\alpha$ (17.4 keV) and $K\beta$ (19.6 keV) lines without filtering, because the metal vapor at the target tip has a strong monochromatic effect.²¹ Therefore, we are very interested in the measurement of the characteristic rays from nickel, copper, silver, cerium, and tungsten targets; the target element should be selected corresponding to the radiographic objectives. In a medical application, K-series characteristic x-rays of cerium are absorbed effec-

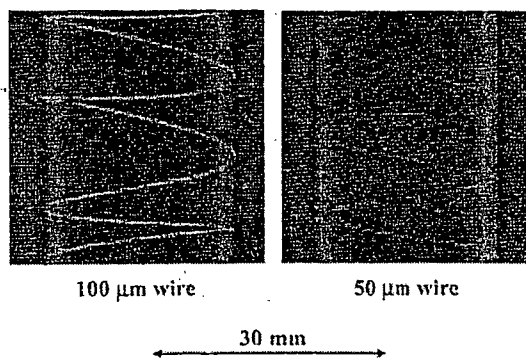


Fig. 8 Radiograms of tungsten wires of 50 and 100 μ m in diameter coiled around a pipe made of polymethyl methacrylate. A 50- μ m-diam wire could be observed.

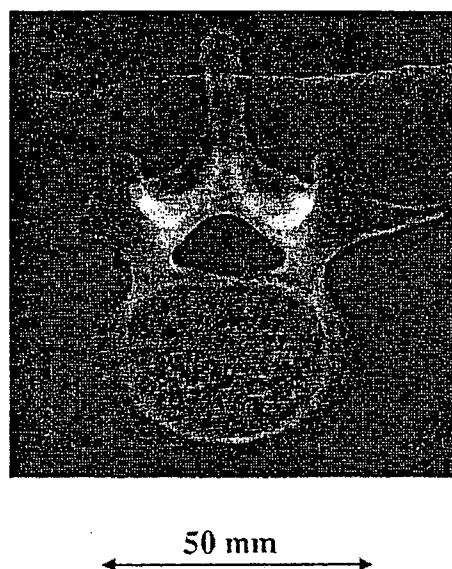


Fig. 9 Radiogram of vertebra. Fine structures of the vertebra were visible.

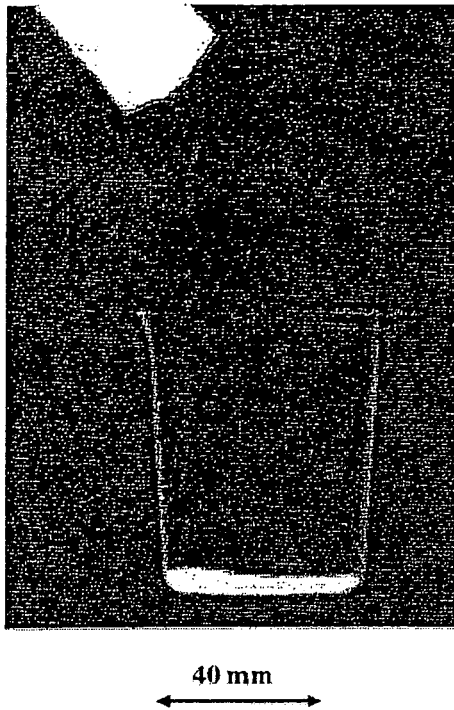


Fig. 10 Radiogram of water spouted from an injector. The stop-motion image of water was obtained by monochromatic flash radiography.

tively by an iodine-based contrast medium with a K-edge of 33.2 keV, and enhanced K-edge angiography can be performed.

In this research, the generator-produced instantaneous number of K photons is approximately 2×10^8 photons/cm² per pulse at 1.0 m from the source. Subsequently, the intensity can be increased by increasing the electrostatic energy in the condenser, and monochromatic K α lines are selected using a zirconium filter with a K-edge of 17.9 keV.

Compared with a triode, the photon energy of K-series characteristic x-rays can be increased, and the pulse widths are shorter. In addition, because sufficient x-ray intensities for CR radiography have been obtained with high dose rates, we plan to design a high-speed photon-counting radiography system to decrease noise from radiograms.

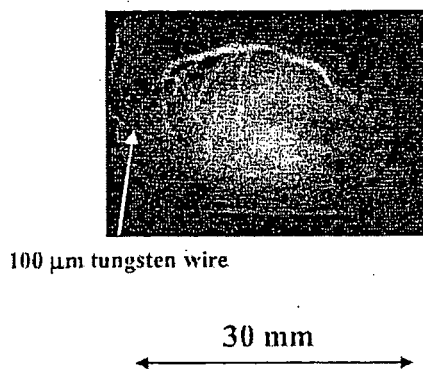


Fig. 11 Angiogram of rabbit heart. Fine blood vessels approximately 100 μ m in diameter were visible.

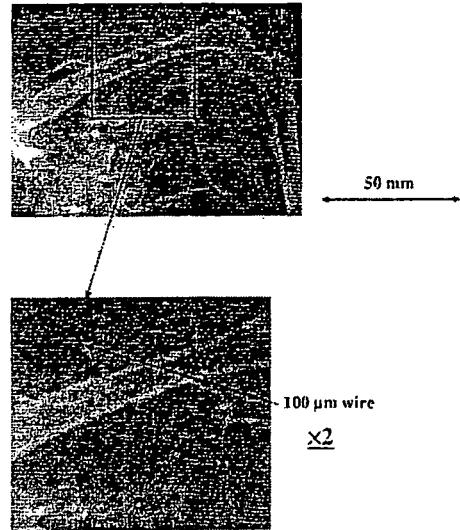


Fig. 12 Angiograms of rabbit thigh. We could see fine blood vessels approximately 100 μ m.

Using this x-ray generator, demonstrations of various monochromatic high-speed radiography will be accomplished easily, since the target element can be changed easily. In addition, steady-state quasi-monochromatic x-ray generators for medical radiography will be developed soon using angular dependence of the bremsstrahlung x-ray intensity distribution. In cases where monochromatic cone beams are employed (because the irradiation field can be increased easily as compared with monochromatic parallel beams using a synchrotron), high-photon-energy enhanced K-edge angiography using a gadolinium-based contrast medium with a K edge of 50.2 keV can be performed, and the absorbed dose during angiography can be decreased easily.

Acknowledgment

This work was supported by Grants-in-Aid for Scientific Research (13470154, 13877114, 16591181, and 16591222) and Advanced Medical Scientific Research from MECSS, Health and Labor Sciences Research Grants (RAMT-nano-001, RHGTEFB-genome-005, and RHGTEFB-saisei-003), grants from the Keiryō Research Foundation, The Promotion and Mutual Aid Corporation for Private Schools of Japan, Japan Science and Technology Agency (JST), and New Energy and Industrial Technology Development Organization (NEDO, Industrial Technology Research Grant Program in 2003).

References

1. H. Mori, K. Hyodo, E. Tanaka, M. U. Mohammed, A. Yamakawa, Y. Shinozaki, H. Nakazawa, Y. Tanaka, T. Sekka, Y. Iwata, S. Honda, K. Umetani, H. Ueki, T. Yokoyama, K. Tanioka, M. Kubota, H. Hosaka, N. Ishizawa, and M. Ando, "Small-vessel radiography in situ with monochromatic synchrotron radiation," *Radiology* 201, 173–177 (1996).
2. K. Hyodo, M. Ando, Y. Oku, S. Yamamoto, T. Takeda, Y. Itai, S. Ohtsuka, Y. Sugishita, and J. Tada, "Development of a two-dimensional imaging system for clinical applications of intravenous coronary angiography using intense synchrotron radiation produced by a multipole wiggler," *J. Synchrotron Radiat.* 5, 1123–1126 (1998).
3. A. Momose, T. Takeda, Y. Itai, and K. Hirano, "Phase-contrast x-ray computed tomography for observing biological soft tissues," *Nat. Med.* 2, 473–475 (1996).
4. M. Ando, A. Maksimenko, H. Sugiyama, W. Pattanasiriwisawa, K.

- Hyodo, and C. Uyama, "A simple x-ray dark- and bright- field imaging using achromatic Laue optics," *Jpn. J. Appl. Phys., Part 2* 41, L1016-L1018 (2002).
5. E. Sato, H. Isobe, and F. Hoshino, "High intensity flash x-ray apparatus for biomedical radiography," *Rev. Sci. Instrum.* 57, 1399-1408 (1986).
 6. E. Sato, S. Kimura, S. Kawasaki, H. Isobe, K. Takahashi, Y. Tamakawa, and T. Yanagisawa, "Repetitive flash x-ray generator utilizing a simple diode with a new type of energy-selective function," *Rev. Sci. Instrum.* 61, 2343-2348 (1990).
 7. E. Sato, M. Sagae, K. Takahashi, T. Oizumi, H. Ojima, K. Takayama, Y. Tamakawa, T. Yanagisawa, A. Fujiwara, and K. Mitoya, "High-speed soft x-ray generators in biomedicine," *Proc. SPIE* 2513, 649-667 (1994).
 8. A. Shikoda, E. Sato, M. Sagae, T. Oizumi, Y. Tamakawa, and T. Yanagisawa, "Repetitive flash x-ray generator having a high-durability diode driven by a two-cable-type line pulser," *Rev. Sci. Instrum.* 65, 850-856 (1994).
 9. E. Sato, K. Takahashi, M. Sagae, S. Kimura, T. Oizumi, Y. Hayasi, Y. Tamakawa, and T. Yanagisawa, "Sub-kilohertz flash x-ray generator utilizing a glass-enclosed cold-cathode triode," *Med. Biol. Eng. Comput.* 32, 289-294 (1994).
 10. K. Takahashi, E. Sato, M. Sagae, T. Oizumi, Y. Tamakawa, and T. Yanagisawa, "Fundamental study on a long-duration flash x-ray generator with a surface-discharge triode," *Jpn. J. Appl. Phys., Part 1* 33, 4146-4151 (1994).
 11. E. Sato, M. Sagae, E. Tanaka, Y. Hayasi, R. Germer, H. Mori, T. Kawai, T. Ichimaru, S. Sato, K. Takayama, and H. Ido, "Quasi-monochromatic flash x-ray generator utilizing a disk-cathode molybdenum tube," *Jpn. J. Appl. Phys., Part 1* 43, 7324-7328 (2004).
 12. E. Sato, Y. Hayasi, R. Germer, E. Tanaka, H. Mori, T. Kawai, H. Obara, T. Ichimaru, K. Takayama, and H. Ido, "Irradiation of intense characteristic x-rays from weakly ionized linear molybdenum plasma," *Jpn. J. Med. Phys.* 23, 123-131 (2003).
 13. E. Sato, Y. Hayasi, R. Germer, E. Tanaka, H. Mori, T. Kawai, T. Ichimaru, K. Takayama, and H. Ido, "Quasi-monochromatic flash x-ray generator utilizing weakly ionized linear copper plasma," *Rev. Sci. Instrum.* 74, 5236-5240 (2003).
 14. E. Sato, R. Germer, Y. Hayasi, Y. Koorikawa, K. Murakami, E. Tanaka, H. Mori, T. Kawai, T. Ichimaru, F. Obata, K. Takahashi, S. Sato, K. Takayama, and H. Ido, "Weakly ionized plasma flash x-ray generator and its distinctive characteristics," *Proc. SPIE* 5196, 383-392 (2003).
 15. E. Sato, Y. Hayasi, R. Germer, H. Obara, E. Tanaka, H. Mori, T. Kawai, T. Inoue, A. Ogawa, S. Sato, K. Takayama, and H. Ido, "Sharp characteristic x-ray irradiation from weakly ionized linear plasma," *J. Electron Spectrosc. Relat. Phenom.* 137(40), 713-720 (2004).
 16. E. Sato, E. Tanaka, H. Mori, T. Kawai, S. Sato, and K. Takayama, "Clean monochromatic x-ray irradiation from weakly ionized linear copper plasma," *Opt. Eng.* 44, 049002-1-6. 2005.
 17. E. Sato, M. Sagae, E. Tanaka, Y. Hayasi, R. Germer, H. Mori, T. Kawai, T. Ichimaru, S. Sato, K. Takayama, and H. Ido, "Quasi-monochromatic flash x-ray generator utilizing a disk-cathode molybdenum tube," *Jpn. J. Appl. Phys., Part 1* 43, 7324-7328 (2004).
 18. E. Sato, E. Tanaka, H. Mori, T. Kawai, T. Ichimaru, S. Sato, K. Takayama, and H. Ido, "Compact monochromatic flash x-ray generator utilizing a disk-cathode molybdenum tube," *Med. Phys.* 32, 49-54 (2005).
 19. E. Sato, K. Sato, and Y. Tamakawa, "Film-less computed radiography system for high-speed imaging," *Ann. Rep. Iwate Med. Univ. Sch. Lib. Arts Sci.* 35, 13-23 (2000).
 20. M. Sagae, E. Sato, E. Tanaka, Y. Hayasi, R. Germer, H. Mori, T. Kawai, T. Ichimaru, S. Sato, K. Takayama, and H. Ido, "Quasi-monochromatic x-ray generator utilizing graphite cathode diode with transmission-type molybdenum target," *Jpn. J. Appl. Phys., Part 1* 44, 446-449 (2005).
 21. H. Obara, E. Sato, Y. Hayasi, E. Tanaka, H. Mori, T. Kawai, T. Inoue, A. Ogawa, S. Sato, T. Ichimaru, K. Takayama, and H. Ido, "Superposition of x-ray spectra using alloy-target plasma triode," *Proc. SPIE* 5920, 59200W-1-8 (2005).

Michiaki Sagae received the BS in applied physics from Tohoku Gakuin University, Sendai, in 1982. Since 1991, he has been a member of the Department of Physics, Iwate Medical University. His interests are in high-speed radiography, vacuum discharges, and image management in biomedical areas.

Eiichi Sato received his BS, MS, and PhD in applied physics from Tohoku Gakuin University, Sendai, Japan, in 1979, 1982, and 1987, respectively. He is currently a professor in the Department of Physics at Iwate Medical University. He has written some 400 publications and delivered some 200 international presentations concerning x-rays. His research interests include soft flash x-ray generators, quasi-x-ray laser generators, and high-speed radiography. In 2000 he received the Schardin Gold Medal from the German Physical Society, in 2003 he received the Takayama Award (Gold Medal) from the Japan Society of High Speed Photography and Photonics, and he received the Honorable Mention Poster Award from the SPIE International Symposium on Medical Imaging 2005.

Etsuro Tanaka received his MD and PhD degrees in medicine from Kumamoto University, Japan, in 1980 and 1986, respectively. He worked on medical image processing in the Department of Physiology, Tokai University, Japan, from 1988 to 2003. He is currently a professor in the Department of Nutritional Sciences, Tokyo University of Agriculture, Japan. His research interests include medical image processing, human physiology, and clinical nutrition.

Hidezo Mori received a medical degree from Keio University School of Medicine, Tokyo, Japan, in 1977, and also a PhD from the Post Graduate School, Keio University School of Medicine. Now he is the director of the Department of Cardiac Physiology at the National Cardiovascular Center, Suita, Japan. His primary research interests are regenerative therapy in cardiovascular disease, microcirculation, and medical applications of structural biology.

Toshiaki Kawai received the BS degree in precision mechanics and the MS degree in electronic engineering from Shizuoka University, Hamamatsu, Japan, in 1964 and 1974, respectively. In 1974, he joined Hamamatsu Photonics K. K., where he worked on the research and development of solid-state infrared detectors. From 1978 to 1981, he engaged in research work on the NEA cold cathode for application to imaging camera tubes. He is now the project coordinator of Electron Tube Division 2 and is engaged in the development and manufacturing of imaging devices and x-ray equipment. He is a member of the Japan Radioisotope Association and the Institute of Image Information and Television Engineers of Japan.

Takashi Inoue received his MD and PhD degrees in 2000 from Tohoku University. He is currently an assistant professor in the Department of Neurosurgery at Iwate Medical University, and a member of the Japan Neurosurgical Society. His research interests include neurosurgery and magnetic resonance imaging.

Akira Ogawa received his MD and PhD degrees in 1981 from Tohoku University. He is currently a professor in the Department of Neurosurgery, dean of the School of Medicine at Iwate Medical University, and is a trustee of the Japan Neurosurgical Society. His research interests include neurosurgery and cerebrovascular disease.

Shigehiro Sato received his MD degree from Iwate Medical University in 1980. He worked for the laboratory of the Division of Pediatric Infectious Diseases at Johns Hopkins Hospital from 1985 to 1989. He is currently a professor in the Department of Microbiology at Iwate Medical University. His research interests include central nervous system damage caused by Vero toxin, a cell culture system for vaccine development, and microangiopathy.

Kazuyoshi Takayama received his BS degree from Nagoya Institute of Technology in 1962. In 1970, he received his PhD in mechanical engineering from Tohoku University. He is currently a director (professor) in the Shock Wave Research Center, Institute of Fluid Science at Tohoku University. His research interests include various shock wave phenomena, high-speed photography, and flash radiography. He has received seven awards including the coveted Ernst Mach Medal in 2000.

Jun Onagawa received his BS and PhD degrees in physics from Tohoku Gakuin University in 1968 and 2001, respectively. He is currently a professor in the Department of Applied Physics and Informatics, Faculty of Engineering, at Tohoku Gakuin University. His research interests include target metallography and x-ray spectroscopy.

Hideaki Ido received his BS, MS, and PhD degrees in physics from Tohoku University in 1962, 1964, and 1967, respectively. He is currently a professor in the Department of Applied Physics and Informatics, Faculty of Engineering, at Tohoku Gakuin University, Japan. His research interests include magnetism and x-ray spectroscopy.

Novel monochromatic x-ray generators and their applications to high-speed radiography

Eiichi Sato^{*a}, Rudolf Germer^b, Haruo Obara^c, Etsuro Tanaka^d, Hidezo Mori^e, Toshiaki Kawai^f, Takashi Inoue^g, Akira Ogawa^g, Mitsuru Izumisawa^h, Toshio Ichimaruⁱ, Kiyomi Takahashi^j, Shigehiro Sato^j and Kazuyoshi Takayama^k

^aDepartment of Physics, Iwate Medical University, 3-16-1 Honchodori, Morioka 020-0015, Japan

^bITP, FHTW FB1 and TU-Berlin, Blankenhainer Str. 9, D 12249 Berlin, Germany

^cDepartment of Radiological Technology, College of Medical Science, Tohoku University, 1-1 Seiryochō, Sendai 980-0872, Japan

^dDepartment of Nutritional Science, Faculty of Applied Bio-science, Tokyo University of Agriculture, 1-1-1 Sakuragaoka, Setagaya-ku 156-8502, Japan

^eDepartment of Cardiac Physiology, National Cardiovascular Center Research Institute, 5-7-1 Fujishirodai, Suita, Osaka 565-8565, Japan

^fElectron Tube Division #2, Hamamatsu Photonics Inc., 314-5 Shimokanzo, Iwata 438-0193, Japan

^gDepartment of Neurosurgery, School of Medicine, Iwate Medical University, 19-1 Uchimaru, Morioka 020-8505, Japan

^hDepartment of Oral Radiology, School of Dentistry, Iwate Medical University, 1-3-27 Chuo, Morioka 020-0021, Japan

ⁱDepartment of Radiological Technology, School of Health Sciences, Hirosaki University, 66-1 Honcho, Hirosaki 036-8564, Japan

^jDepartment of Microbiology, School of Medicine, Iwate Medical University, 19-1 Uchimaru, Morioka 020-8505, Japan

^kTohoku University Biomedical Engineering Research Organization, 2-1-1 Katahira, Sendai 980-8577, Japan

ABSTRACT

Novel monochromatic x-ray generators and their applications to high-speed radiography are described. The five generators are as follows: a weakly ionized linear plasma x-ray generator, a monochromatic compact flash x-ray generator, a super-fluorescent plasma generator, a cerium x-ray generator using a 3.0-mm-thick aluminum filter, and a 100- μm -focus x-ray generator utilizing the filter. Using the linear plasma generator with a copper target, we observed clean K lines and their harmonics, and soft flash radiography was performed with pulse widths of approximately 500 ns. The compact monochromatic flash x-ray generator produced clean molybdenum K lines easily, and high-speed radiography was performed with pulse widths of approximately 100 ns. Using a steady-state cerium x-ray generator, we performed real-time angiography utilizing an image intensifier and a high-sensitive camera (MLX) made by NAC Image Technology Inc. with a capture time of 1 ms. Finally, real-time magnification radiography was performed by twofold magnification imaging using a 100- μm -focus x-ray generator and the high-sensitive camera.

Keywords: flash radiography, high-speed radiography, high-speed angiography, real-time radiography, enhanced K-edge angiography, high-sensitive CCD camera, image intensifier

1. INTRODUCTION

Conventional flash x-ray generators utilizing high-voltage condensers have been used in high-speed radiography,¹ and single generators have been employed to perform delayed radiography using a trigger delay device. Subsequently, plural flash x-ray generators can be combined to a multi-tube (anode) flash x-ray system to perform extremely high-repetition-rate radiography and multi-direction radiography at desired times. Subsequently, we have developed several different flash x-ray generators²⁻⁵ with photon energies of lower than 150 keV, and these generators have been employed to soft radiography including biomedical applications.

Stroboscopic x-ray generators⁶⁻⁸ have been developed to primarily perform single and multi-shot radiography using an x-ray film or a computed radiography (CR) system,⁹ therefore high-speed real-time radiography can be achieved with a high-speed camera. Although we have developed three stroboscopic generators, major advantages are as follows: maximum repetition rate of approximately 100 kHz, variable x-ray duration, and low noises. Using a special high-voltage pulse generator, the maximum rate can be increased to 1 MHz or beyond.

Recently, we have developed three monochromatic flash x-ray generators¹⁰⁻¹⁸ in order to produce clean K-series characteristic x-rays. The major goal of these developments is to produce slightly coherent clean K lines by x-ray amplification of spontaneous emission of radiation and by increasing the flux of K lines in the plasma. In view of this situation, we have confirmed the irradiation of clean K lines and their harmonics from weakly ionized linear plasmas of nickel and copper.

To perform iodine K-edge angiography using cone beams, we have developed a steady-state cerium x-ray generator¹⁹⁻²¹ and have succeeded in observing fine blood vessels and coronary arteries with high contrasts using cerium K lines. Recently, because an extremely high-sensitive CCD camera (MLX) with variable capture times has been developed by NAC Image Technology Inc., stop-motion images can be easily obtained.

Magnification radiography²² is useful in order to improve the spatial resolution in digital radiography, and narrow-photon-energy bremsstrahlung x-rays with a peak energy of approximately 35 keV from a microfocus tungsten tube are useful for performing high-contrast high-resolution angiography. In magnification radiography, scattering beams from radiographic objects can be reduced without using a grid, and stop-motion images can be taken using the CCD camera.

In this paper, we introduce novel monochromatic x-ray generators, their distinctive radiographic characteristics, and applications to high-speed radiographies including enhanced K-edge angiography.

2. WEAKLY IONIZED LINEAR PLASMA X-RAY GENERATOR

2.1 Generator

Figure 1 shows a block diagram of a high-intensity plasma flash x-ray generator. This generator consists of the following essential components: a high-voltage power supply, a high-voltage condenser with a capacity of approximately 200 nF, a turbomolecular pump, a krytron pulse generator as a trigger device, and a flash x-ray tube. The high-voltage main condenser is charged to 50 kV by the power supply, and electric charges in the condenser are discharged to the tube after triggering the cathode electrode with the trigger device. The plasma flash x-rays are then produced.

The x-ray tube is a demountable cold-cathode triode that is connected to the turbomolecular pump with a pressure of approximately 1 mPa. This tube consists of the following major parts: a hollow cylindrical carbon cathode with a bore diameter of 10.0 mm, a brass focusing electrode, a trigger electrode made from copper wire, a stainless steel vacuum chamber, a nylon insulator, a polyethylene terephthalate (Mylar) x-ray window 0.25 mm in thickness, and a rod-shaped copper target 3.0 mm in diameter with a tip angle of 60°. The distance between the target and cathode electrodes is approximately 20 mm, and the trigger electrode is set in the cathode electrode. As electron beams from the cathode electrode are roughly converged to the target by the focusing electrode, evaporation leads to the formation of a weakly ionized linear plasma, consisting of copper ions and electrons, around the fine target.

In the linear plasma, bremsstrahlung photons with energies higher than the K-absorption edge are effectively absorbed and are converted into fluorescent x-rays. The plasma then transmits the fluorescent rays easily, and bremsstrahlung rays with energies lower than the K-edge are also absorbed by the plasma. In addition, because bremsstrahlung rays are not emitted in the opposite direction to that of electron trajectory, intense characteristic x-rays are generated from the plasma-axial direction.

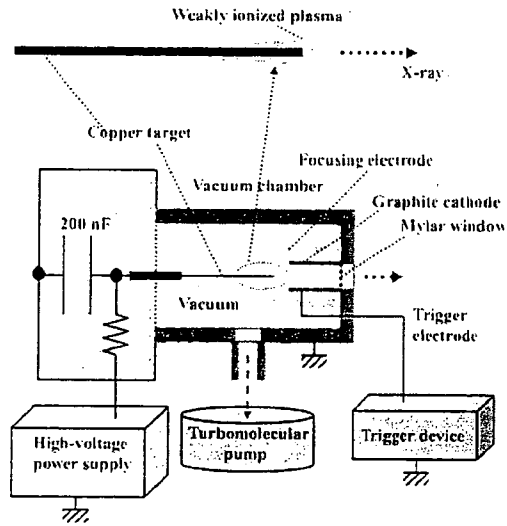


Fig. 1. Block diagram of the weakly ionized linear plasma x-ray generator.

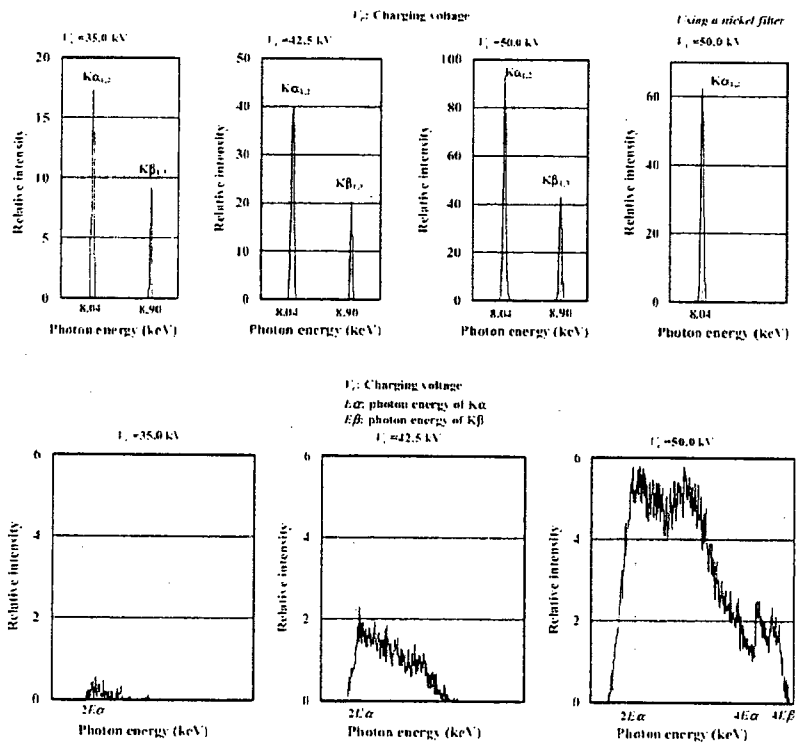


Fig. 2. X-ray spectra from weakly ionized linear copper plasma.

2.2 Characteristics

In the flash x-ray generators, the tube voltage and current were measured by a high-voltage divider and a current

transformer, respectively. The tube voltage and current displayed damped oscillations. At a charging voltage of 50 kV, the maximum tube voltage was almost equal to the charging voltage of the main condenser, and the peak current was about 16 kA.

The x-ray pulse widths were approximately 300 ns, and the time-integrated x-ray intensity had a value of approximately 1.5 mGy per pulse at 1.0 m from the x-ray source with a charging voltage of 50 kV.

X-ray spectra from the plasma source were measured by a transmission-type spectrometer with a lithium fluoride curved crystal 0.5 mm in thickness. The spectra were taken by the CR system (Konica Regius 150), and relative x-ray intensity was calculated from Dicom digital data. Figure 2 shows measured spectra from the copper target at the indicated conditions. In fact, we observed clean K lines, and $K\alpha$ lines were left by absorbing $K\beta$ lines using a 10- μm -thick nickel filter. The characteristic x-ray intensity substantially increased with corresponding increases in the charging voltage, and higher harmonic hard x-rays were observed.

2.3 High-speed radiography

The plasma radiography was performed by the CR system using the filter. The charging voltage and the distance between the x-ray source and imaging plate were 50 kV and 1.2 m, respectively.

First, rough measurements of spatial resolution were made using wires. Radiograms of tungsten wires coiled around pipes made of polymethyl methacrylate (PMMA) are shown in Fig. 3. Although the image contrast decreased somewhat with decreases in the wire diameter, due to blurring of the image caused by the sampling pitch of 87.5 μm , a 50- μm -diameter wire could be observed. Figure 4 shows a radiogram of plastic bullets falling into a polypropylene beaker from a plastic test tube. Because the x-ray duration was about 500 ns, the stop-motion image of bullets could be obtained.

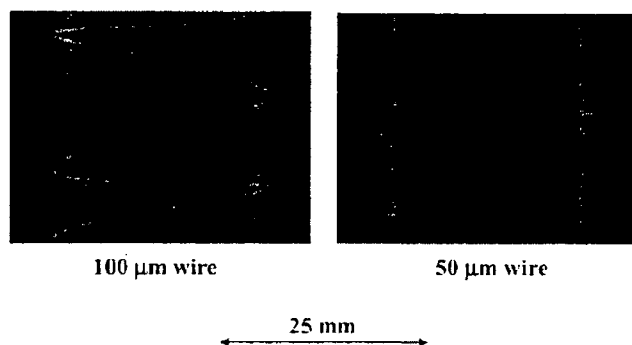


Fig. 3. Radiograms of tungsten wires coiled around pipes made of polymethyl methacrylate (PMMA).

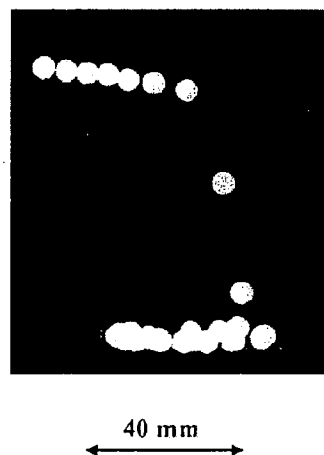


Fig. 4. Radiogram of plastic bullets falling into a polypropylene beaker from a plastic test tube.

3. COMPACT MONOCHROMATIC FLASH X-RAY GENERATOR

3.1 Generator

Figure 5 shows a block diagram of a compact monochromatic flash x-ray generator. This generator consists of the following components: a constant high-voltage power supply, a surge Marx generator with a capacity during main discharge of 425 pF, a thyatron trigger device of the surge generator, a turbomolecular pump, and a flash x-ray tube. Since the electric circuit of the high-voltage pulse generator employs a polarity-inversion two-stage Marx line, the surge generator produces twice the potential of the condenser charging voltage. When two condensers inside of the surge generator are charged from -50 to -70 kV, the ideal output voltage ranges from 100 to 140 kV.

The x-ray tube is a demountable diode type, as illustrated in Fig. 6. This tube is connected to the turbomolecular pump with a pressure of about 1 mPa and consists of the following major devices: a rod-shaped molybdenum target 3.0 mm in diameter, a disk cathode made of graphite, a polyethylene terephthalate (Mylar) x-ray window 0.25 mm in thickness, and a polymethyl methacrylate (PMMA) tube body. The target-cathode space was regulated to 1.0 mm from the outside of the x-ray tube by rotating the anode rod, and the transmission x-rays are obtained through a 1.0-mm-thick graphite cathode and an x-ray window. Because bremsstrahlung rays are not emitted in the opposite direction to that of electron trajectory, molybdenum $K\alpha$ rays can be produced using a 20- μm -thick zirconium K-edge filter.

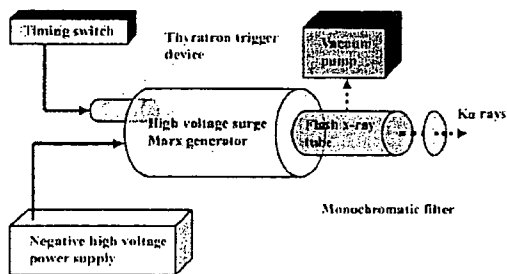


Fig. 5. Block diagram of the compact monochromatic flash x-ray generator.

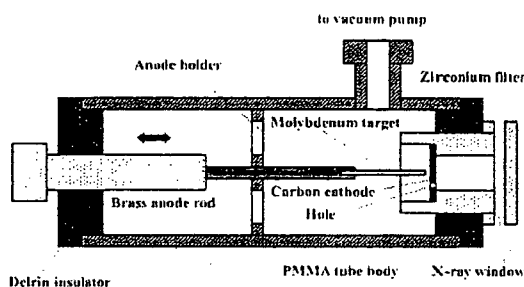


Fig. 6. Structure of the monochromatic flash x-ray tube with a PMMA tube body.

3.2 Characteristics

At a charging voltage of -70 kV, the maximum tube voltage and current were 120 kV and 1.0 kA, respectively. The x-ray pulse widths were approximately 70 ns, and the $K\alpha$ intensity was approximately 70 μGy per pulse at 0.5 m from the source of 3.0 mm in diameter. In the spectrum measurement, clean molybdenum $K\alpha$ lines were left using the zirconium filter, and the K-ray intensity substantially increased with increasing the charging voltage (Fig. 7).

3.3 High-speed radiography

The monochromatic flash radiography was performed by the CR system at 0.5 m from the x-ray source with the filter, and the charging voltage was -70 kV. The radiogram of water falling into a polypropylene beaker from a glass test tube is shown in Fig. 8. This image was taken with the slight addition of an iodine-based contrast medium. Because the x-ray duration was about 100 ns, the stop-motion image of water could be obtained.

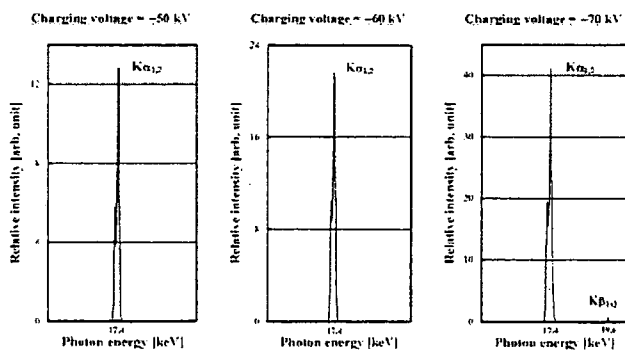


Fig. 7. X-ray spectra from the monochromatic flash x-ray tube with a molybdenum target.



Fig. 8. Radiogram of water falling into a polypropylene beaker from a glass test tube.

4. SUPER-FLUORESCENT PLASMA X-RAY GENERATOR

4.1 Generator

Figure 9 shows a block diagram of a high-intensity super-fluorescent plasma flash x-ray generator. The generator consists of the following essential components: a high-voltage power supply, a high-voltage condenser with a capacity of approximately 150 nF, an air gap switch, a turbomolecular pump, a thyatron pulse generator as a trigger device, and a flash x-ray tube. In this generator, a coaxial cable transmission line is employed in order to increase maximum tube voltage using high-voltage reflection. The high-voltage main condenser is charged up to 80 kV by the power supply, and electric charges in the condenser are discharged to the tube through the four cables after closing the gap switch with the trigger device.

The x-ray tube is a demountable cold-cathode diode that is connected to the turbomolecular pump with a pressure of approximately 1 mPa. This tube consists of the following major parts: a ring-shaped graphite cathode with an inside diameter of 4.5 mm, a stainless-steel vacuum chamber, a nylon insulator, a polyethylene terephthalate (Mylar) x-ray window 0.25 mm in thickness, and a rod-shaped tungsten target 3.0 mm in diameter. The distance between the target and cathode electrodes can be regulated from the outside of the tube, and is set to 1.5 mm. As electron beams from the cathode electrode are roughly converged to the target by the electric field in the tube, evaporation leads to the formation of weakly ionized plasma, consisting of tungsten ions and electrons, at the target tip. Because bremsstrahlung rays are not emitted in the opposite direction to that of electron trajectory, tungsten $K\alpha$ lines are left by absorbing $K\beta$ lines using an ytterbium oxide filter.

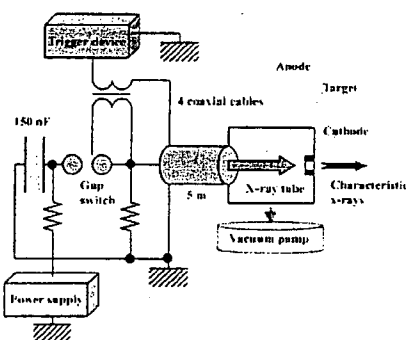


Fig. 9. Block diagram of the high-intensity super-fluorescent plasma flash x-ray generator

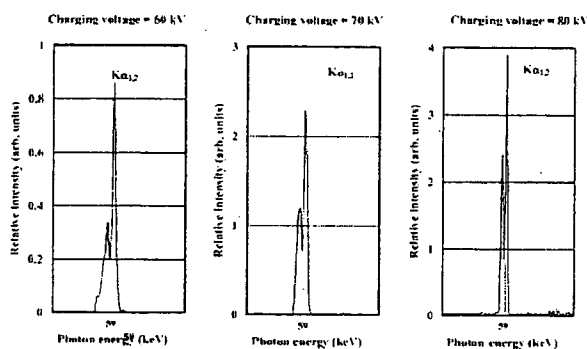


Fig. 10. X-ray spectra from the super-fluorescent plasma x-ray tube with a tungsten target.

4.2 Characteristics

Since the electric circuit of the high-voltage pulse generator employs a cable transmission line, the high-voltage pulse generator produces twice the potential of the condenser charging voltage. At a charging voltage of 80 kV, the estimated maximum tube voltage and current are approximately 160 kV and 40 kA, respectively. The x-ray pulse widths were approximately 110 ns, and the time-integrated x-ray intensity had a value of approximately 50 μGy at 1.0 m from the x-ray source with a charging voltage of 80 kV using the filter. When the charging voltage was increased using the filter, the characteristic x-ray intensities of tungsten $K\alpha$ lines increased. The $K\alpha$ lines were clean, and hardly any $K\beta$ lines and bremsstrahlung rays were detected (Fig. 10).

4.3 High-speed gadolinium K-edge angiography

Figure 11 shows the mass attenuation coefficients of gadolinium at the selected energies; the coefficient curve is discontinuous at the gadolinium K-edge. The average photon energy of the tungsten $K\alpha$ lines is shown just above the gadolinium K-edge. The average photon energy of tungsten $K\alpha$ lines is 58.9 keV, and gadolinium contrast media with a K-absorption edge of 50.2 keV absorb the lines easily. Therefore, blood vessels were observed with high contrasts. The flash angiography was performed by the CR system at 1.2 m from the x-ray source, and the charging voltage was 70 kV. Figure 12 shows angiogram of a rabbit head using gadolinium oxide powder, and fine blood vessels of approximately 100 μm were visible.

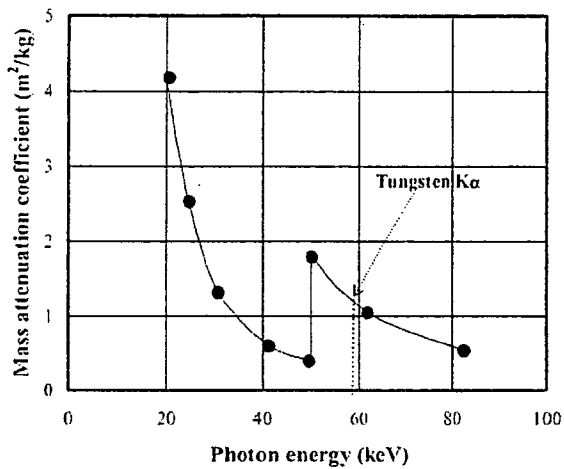


Fig. 11. Mass attenuation coefficients of gadolinium and the average photon energy of the tungsten $K\alpha$ lines.

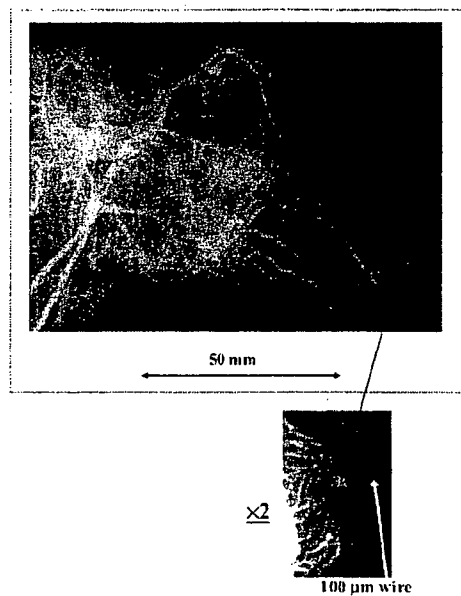


Fig. 12. Angiogram of a rabbit head using gadolinium oxide powder.

5. CERIUM X-RAY GENERATOR

5.1 Generator

The main circuit for producing x-rays is illustrated in Fig. 13, and employed the Cockcroft-Walton circuit in order to decrease the dimensions of the tube unit. In the x-ray tube, the negative high voltage is applied to the cathode electrode, and the anode (target) is connected to the tube unit case (ground potential) to cool the anode and the target effectively. The filament heating current is supplied by an AC power supply in the controller in conjunction with an insulation transformer. In this experiment, the tube voltage applied was from 45 to 65 kV, and the tube current was regulated to within 0.40 mA (maximum current) by the filament temperature. The exposure time is controlled in order to obtain optimum x-ray intensity. Quasi-monochromatic x-rays are produced using a 3.0-mm-thick aluminum filter for absorbing soft bremsstrahlung rays.

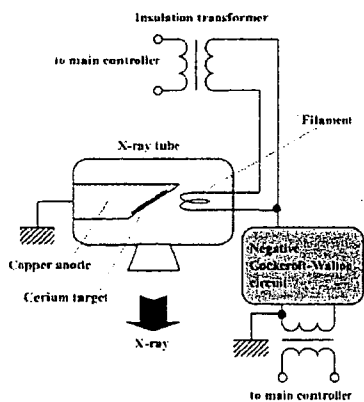


Fig. 13. Main high-voltage transmission line of the cerium x-ray generator.

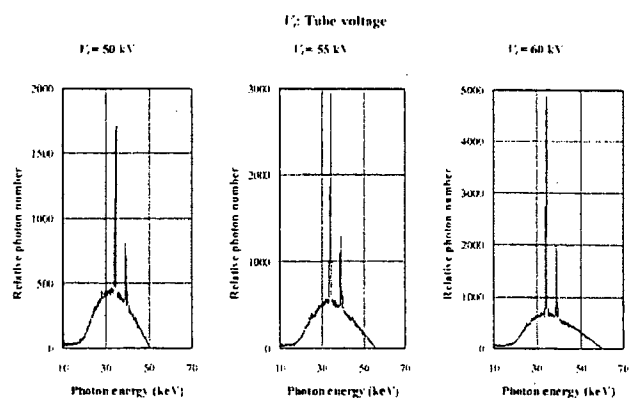


Fig. 14. X-ray spectra using a 3.0-mm-thick aluminum filter with changing the tube voltage.

5.2 Characteristics

The maximum tube voltage and current were 65 kV and 0.4 mA, respectively, and the focal-spot sizes were 1.3×0.9 mm. Cerium K-series characteristic x-rays were left using a 3.0 mm-thick aluminum filter (Fig. 14), and the x-ray intensity was 19.9 μGy/s at 1.0 m from the source with a tube voltage of 60 kV and a current of 0.40 mA.

5.3 High-speed radiography

Real-time cohesion radiography was performed using an image intensifier (I I) and a high-sensitive CCD camera (MLX) made by NAC Image Technology at a frame speed of 30 Hz and an image capture time (shutter speed) of 1 ms (Fig. 15). Radiograms from the I I are taken by the CCD camera, and digital video files are recorded by a personal computer through a video capture box.

Figure 16 shows the mass attenuation coefficients of iodine at the selected energies; the coefficient curve is discontinuous at the iodine K-edge. The average photon energy of the cerium Kα lines is shown just above the iodine K-edge. The average photon energy of Kα lines is 34.6 keV, and iodine contrast media with a K-absorption edge of 33.2 keV absorb the lines easily. Therefore, blood vessels were observed with high contrasts.

Figure 17 shows two frames (angiograms) of water falling into polypropylene beaker from a plastic test tube. These images were taken with a tube voltage of 60 kV, and an iodine-based contrast medium was added a little. Because the capture time was about 1 ms, the stop-motion images of water were obtained. Therefore, blood vessels can be seen with high contrasts.

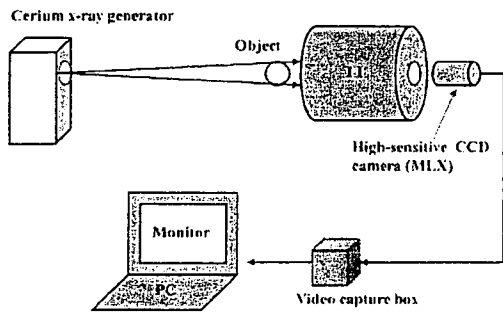


Fig. 15. Experimental setup for performing real-time radiography with a short capture time utilizing an image intensifier and the MLX camera.

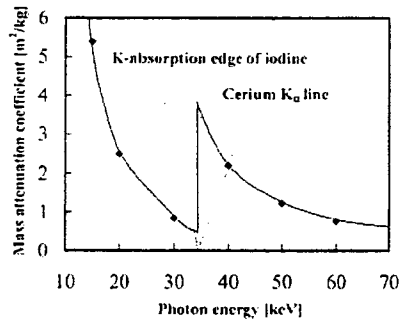


Fig. 16. Mass attenuation coefficients of iodine at the selected energies and the average photon energy of the cerium Kα lines.

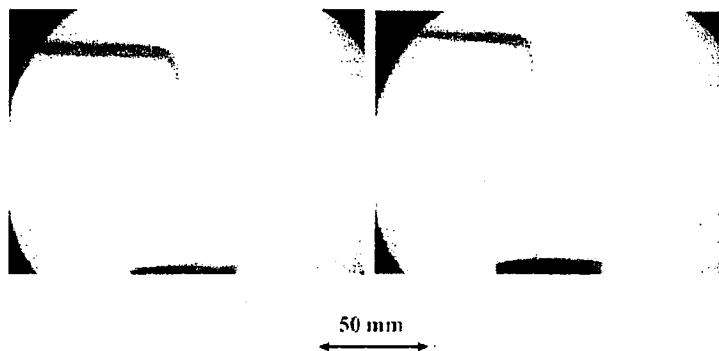


Fig. 17. Two angiograms (frames) of water falling into a polypropylene beaker from a plastic test tube using an iodine medium.

